Tailoring Laser-Generated Plasmas for Efficient Nuclear Excitation by Electron Capture

Yuanbin Wu,* Jonas Gunst,† Christoph H. Keitel, and Adriana Pálffy‡
Max-Planck-Institut für Kernphysik, Saupfercheckweg 1, D-69117 Heidelberg, Germany

(Received 11 August 2017; revised manuscript received 6 November 2017; published 2 February 2018)

The optimal parameters for nuclear excitation by electron capture in plasma environments generated by the interaction of ultrastrong optical lasers with solid matter are investigated theoretically. As a case study we consider a 4.85 keV nuclear transition starting from the long-lived ^{93m}Mo isomer that can lead to the release of the stored 2.4 MeV excitation energy. We find that due to the complex plasma dynamics, the nuclear excitation rate and the actual number of excited nuclei do not reach their maximum at the same laser parameters. The nuclear excitation achievable with a high-power optical laser is up to twelve and up to six orders of magnitude larger than the values predicted for direct resonant and secondary plasma-mediated excitation at the x-ray free electron laser, respectively. Our results show that the experimental observation of the nuclear excitation of ^{93m}Mo and the subsequent release of stored energy should be possible at laser facilities available today.

DOI: 10.1103/PhysRevLett.120.052504

Novel coherent light sources open unprecedented possibilities for the field of laser-matter interactions [1]. The X-ray Free Electron Laser (XFEL) [2,3] for instance can drive low-energy electromagnetic transitions in nuclei. Ultrastrong optical laser systems with up to a few petawatt power [4–8] are very efficient in generating plasma environments [9] that host complex interactions between photons, electrons, ions, and the atomic nucleus. Nuclear excitation in laser-generated hot plasmas involving optical lasers [10–26], or cold high-density plasmas [27] at the XFEL [28,29], have been under investigation. Special attention has been attracted by nuclear transitions starting from long-lived excited states. Such states are also known as nuclear isomers, and they are particularly interesting due to their potential to store large amounts of energy over long periods of time [30–37]. A typical example is ^{93m}Mo at 2.4 MeV, for which an additional excitation of only 4.85 keV could lead to the depletion of the isomer and release the stored energy on demand.

For both optical and x-ray laser-generated plasmas, the process of nuclear excitation by electron capture (NEEC) [38,39] into the atomic shell has proven to have a significant contribution. As secondary process in the cold plasma environment generated by the interaction of the XFEL with solid-state targets, NEEC can exceed the direct nuclear photoexcitation by six orders of magnitude [28,29] for the 4.85 keV excitation starting from the ^{93m}Mo isomeric state. In this Letter, we show that by tailoring optical-laser-generated plasmas to harness maximum nuclear excitation via NEEC, a further six orders of magnitude increase in the nuclear excitation and subsequent isomer depletion can be reached compared to the case of cold XFEL-generated plasmas. As an interesting point, we find that due to the complexity of the processes involved, the plasma and correspondingly laser parameters for reaching the maximal NEEC rate are not identical to the ones that provide the maximal number of nuclei that are actually excited. Our calculations demonstrate that the maximal number of depleted isomers for realistic laser setup parameters may, for the first time, reach measurable values. Although still far from the final goal, this is a further milestone on the way to the realization of controlled energy storage and release via nuclear isomers.

We consider a strong optical laser that interacts with a solid-state target containing a fraction of nuclei in the isomeric state. NEEC and photoexcitation may occur in the generated plasma. In the resonant process of NEEC, a free electron recombines into a vacant bound atomic state with the simultaneous excitation of the nucleus. The isomers can then be excited to a trigger state that rapidly decays to the nuclear ground state and releases the stored energy. In the following, we consider the case of ^{93m}Mo, for which recent claims have been made [40] on the first observation of NEEC following the proposals in Refs. [41,42].

Free electrons in the plasma cover a broad energy range such that many NEEC resonance channels may contribute to the net NEEC rate λ_{neec}. This can be expressed as the convolution over the electron energy E of the almost Dirac-deltalike NEEC single-resonance cross section σ_{neec} and the free-electron flux ϕ_e, summed over all charge states q and capture channels α_d,

$$\lambda_{\mathrm{neec}}(T_e, n_e) = \sum_{q,\alpha_d} P_q(T_e, n_e) \int dE\, \sigma_{\mathrm{neec}}(E) \phi_e(E, T_e, n_e). \tag{1}$$

Here, P_q is the probability to find ions of charge state q in the plasma as a function of electron temperature T_e and

density n_e. The dependence $\phi_e(T_e)$ determines the quantitative contribution of the NEEC resonances. The theoretical formalism for the calculation of the NEEC cross section σ_{neec} has been presented elsewhere [28,29,43,44]. The total NEEC excitation number N_{exc} is connected to the rate λ_{neec} via

$$N_{\mathrm{exc}} = \int_{V_p} d^3\mathbf{r} \int dt\, n_{\mathrm{iso}}(\mathbf{r}, t)\lambda_{\mathrm{neec}}(T_e, n_e; \mathbf{r}, t), \quad (2)$$

where n_{iso} denotes the number density of isomers and V_p is the plasma volume. Let us assume in a first approximation homogeneous plasma conditions over the plasma lifetime τ_p. Then the total number of excited nuclei is $N_{\mathrm{exc}} = N_{\mathrm{iso}}\lambda_{\mathrm{neec}}(T_e, n_e)\tau_p$, with N_{iso} the number of isomers in the plasma. Assuming a spherical plasma, the plasma lifetime is approximatively given by $\tau_p = R_p\sqrt{m_i/(T_e\bar{Z})}$ [29,45] with the ion mass m_i, the average charge state $\bar{Z}$, and the plasma radius R_p. N_{iso} can be estimated introducing the isomer fraction embedded in the original solid-state target f_{iso}, $N_{\mathrm{iso}} = f_{\mathrm{iso}} n_i V_p$, where n_i stands for the ion number density in the plasma. A $^{93\mathrm{m}}$Mo isomer fraction of $f_{\mathrm{iso}} \approx 10^{-5}$ embedded in solid-state Niobium foils can be generated by intense ($\geq 10^{14}$ protons/s) beams [28] via the $^{93}_{41}\mathrm{Nb}(p,n)^{93\mathrm{m}}_{42}\mathrm{Mo}$ reaction [46].

Numerical results for λ_{neec} and the corresponding total number of excited isomers N_{exc} for an arbitrary plasma radius of 40 μm are presented in Fig. 1. For the calculation of σ_{neec}, we use a theoretical prediction for the reduced nuclear transition probability [47]. We model the plasma conditions by a relativistic distribution for the free electrons and a charge state distribution computed with the radiative-collisional code FLYCHK [48]. The relativistic electronic wave functions [49] and binding energies are in first approximation calculated independently of T_e and n_e, which are accounted for only indirectly via the charge state distribution. For a specific charge state, we further assume that the ion is in its ground state, and the recombination of the NEEC electron occurs in a free orbital. Among these assumptions, neglecting the plasma-induced ionization potential depression [50] is the most severe approximation, as binding energies may vary by few eV to hundreds of eV, depending on the plasma density. Using the Steward-Pyatt model [50] which, for our purpose, also has reasonable agreement with more recently developed methods [51,52], we estimate that the consequences for N_{exc} are even for the case of high-density plasmas with large ionization potential depression only on the level of 10%.

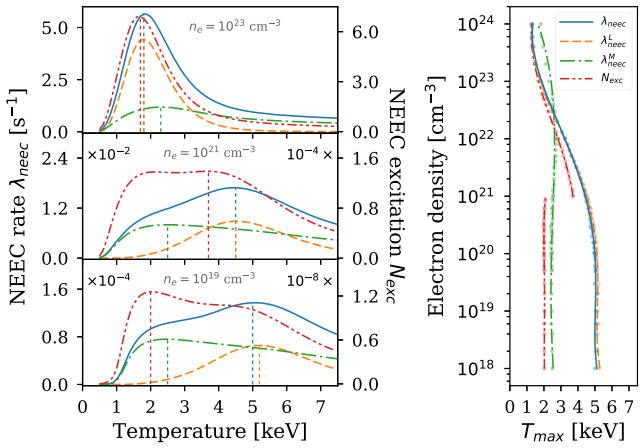

FIG. 1. Left graph: NEEC rate λ_{neec} (blue, solid curve) and the total number of excited isomers N_{exc} (red, dash-dotted curve), as well as the individual contributions $\lambda^L_{\mathrm{neec}}$ (orange, dashed curve) and $\lambda^M_{\mathrm{neec}}$ (green, dash-dotted curve) from the L and M shell, respectively, as a function of the electron temperature T_e for selected electron densities n_e. A plasma radius of 40 μm has been assumed in the calculations of N_{exc}. Right graph: Temperatures T_{max} as functions of density, for maximizing N_{exc}, λ_{neec}, $\lambda^L_{\mathrm{neec}}$ and $\lambda^M_{\mathrm{neec}}$, respectively, at each particular n_e.

NEEC into the K shell is energetically forbidden for the 4.85 keV transition in Mo. The results for the dominant recombination channels into the L and M atomic shells are presented individually in Fig. 1. For the total NEEC rate λ_{neec}, further smaller contributions from the recombination into the N and O shells were also taken into account. Both λ_{neec} and N_{exc} increase with increasing electron density n_e. In the range $n_e = 10^{19}$ cm^{-3} to 10^{20} cm^{-3}, our calculations show that the charge state distribution P_q is nearly unaffected for a fixed temperature T_e, while λ_{neec} is enhanced by a factor of 10, maintaining the same functional dependence on T_e. This indicates that at low densities, the boost in λ_{neec} is (almost) a pure density effect coming from the increasing number of free electrons present in the plasma ($\phi_e \propto n_e$). Increasing the electron density to even higher values, the behavior of λ_{neec} and N_{exc} becomes more involved as the charge distribution P_q shows a complex dependence on the plasma conditions n_e and T_e. Between $n_e = 10^{21}$ cm^{-3} and 10^{23} cm^{-3}, we see that with increasing n_e, the atomic shell contributions change significantly and λ_{neec} is much enhanced.

The temperature T_{max} at which N_{exc} or the total or partial shell contributions λ_{neec} reach a maximum for each density value n_e is depicted in the right graph of Fig. 1. Naively, one would expect that T_{max} is approximately the same for N_{exc} and for λ_{neec}. However, this is only true at high densities starting from 10^{21} cm^{-3}. According to our approximation for τ_p, the chosen plasma lifetime is T_e-dependent. In particular, at low electron densities, τ_p acts as a weighting function proportional to $(T_e)^{-1/2}$ shifting the maximum of N_{exc} to lower temperatures. The optimal plasma conditions for the total excitation number can, thus, drastically differ from the optimal conditions for λ_{neec} in this model. We note that the arbitrary choice of R_p only influences the absolute scale of the NEEC excitation number, not the position of T_{max}.

A comparison with nuclear photoexcitation, assuming a black-body radiation spectrum at the given plasma temperature T_e, shows that at $n_e = 10^{21}$ cm^{-3} NEEC dominates for $T_e < 1.6$ keV and for higher densities $n_e = 10^{22}$ cm^{-3} up to a temperature of 5 keV. The actual photoexcitation in the plasma should be even lower, in particular, at low densities because photons may escape the finite plasma volume easier. For the high density $n_e \geq 10^{23}$ cm^{-3} parameter regime, NEEC is the dominant nuclear excitation mechanism.

In the following, we proceed to determine how the optimal NEEC parameter region in the temperature-density landscape may be accessed by a short laser pulse. In our treatment, we discern two cases, namely the low- and high-density plasmas, and refine our plasma model accordingly. First, we consider the case of a low density (underdense) plasma, which can be generated via the interaction of a strong optical laser with a thin target. The plasma generation process typically evolves in two steps [53]: (i) a preplasma is formed by the prepulse of the laser; (ii) this preplasma is subsequently heated by the main laser pulse, potentially up to keV electron energies.

We model the plasma following the approach in Refs. [53,54]. With the help of the so-called scaling law, the electron temperature is given as $T_e \approx 3.6 I_{16} \lambda_\mu^2$ keV, where I_{16} is the laser intensity in units of 10^{16} W/cm^2 and λ_μ the wavelength in microns [55–57]. The electron density can be estimated as $n_e = N_e/V_p$, where N_e is the total number of electrons and the plasma volume is given by $V_p = \pi R_{\text{focal}}^2 d_p$, with R_{focal} the focal radius of the laser and the plasma thickness $d_p = c\tau_{\text{pulse}}$ determined by the speed of light c and the laser pulse duration τ_{pulse}. The electron number can be related to the absorbed laser energy fE_{pulse} via $N_e = fE_{\text{pulse}}/T_e$. Since experimental results in Refs. [58,59] show that the laser absorption is almost independent of the target material and thickness, we adopt a universal absorption coefficient $f = f(I, \lambda)$, which is a cubic interpolation to theoretical results based on a Vlasov-Fokker-Planck code presented in Ref. [58]. For the considered intensity range between 10^{15} and 2×10^{16} W/cm^2, the absorption fraction f lies between 0.1 and 0.2.

For the cases of focal radius, plasma thickness, and plasma radius of a similar scale, we may again consider the spherical plasma model with the lifetime τ_p. We use the smallest length scale out of R_{focal} and d_p to calculate τ_p for a lower-limit estimate of the NEEC excitation. Numerical results for λ_{neec} and for the total excitation number N_{exc} per laser pulse are presented in Fig. 2 as a function of the laser intensity. We consider a pulse energy of 100 J, wavelength of 1053 nm, and laser pulse duration values of 100, 500, and 1000 fs, respectively. Also here, the optimal laser intensities I_{opt}, at which λ_{neec} and, respectively, N_{exc} are maximal, do not coincide. For the assumed laser parameters, λ_{neec} is maximized by $I_{\text{opt}} = 1.3 \times 10^{16}$ W/cm^2 at a

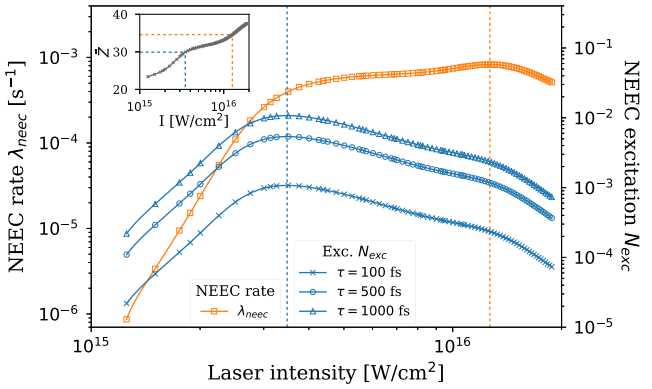

FIG. 2. The NEEC rate λ_{neec} and the total excitation number N_{exc} per laser pulse as functions of laser intensity. The inset shows the average charge state $\bar{Z}$ calculated with the help of FLYCHK. See text for further explanations.

temperature of 5.1 keV and a density of 5.9×10^{19} cm^{-3}. In contrast, the optimal intensity for N_{exc} per laser pulse is 3.5×10^{15} W/cm^2 independent of the laser pulse duration in the range of the considered values. The electron temperature and density achieved at this intensity are 1.4 keV and 6.6×10^{19} cm^{-3}, respectively, leading to a charge state distribution with $\bar{Z} \sim 30$ (see inset of Fig. 2) where capture channels into the M shell still exceed the L-shell contribution. For $d_p < R_{\text{focal}}$ (the case for the parameters of Fig. 2) the plasma lifetime is determined by d_p and in turn by τ_{pulse}. The NEEC excitation becomes stronger with increasing laser pulse duration τ_{pulse} reaching its maximum at the value where $d_p = R_{\text{focal}}$. For even longer pulse durations, we need to use R_{focal} in our model to determine the plasma lifetime and this leads to a decrease of λ_{neec}.

In Table I, we evaluate the optimal laser intensity I_{opt} and the expected maximal NEEC excitation N_{exc} for realistic parameters of high-power optical lasers that are currently available or under construction. The excitation N_{exc} per laser pulse is up to six orders of magnitude larger than the one ($\sim 10^{-6}$, recalculated for the parameters considered here) in the XFEL-generated cold ($T = 350$ eV) plasma [28,29]. The largest value of 1.9 excitations per pulse should be reached with the PETAL laser, which provides both high laser power and long pulse duration.

TABLE I. Laser parameters and maximal N_{exc} achieved at the optimal laser intensity $I_{\text{opt}} = 3.5 \times 10^{15}$ W/cm^2 for ELI-beamlines L4 [4], PETAL [5,6], LULI [7] and VULCAN [8] lasers.

	ELI-beamlines	PETAL	LULI	VULCAN
E_{pulse} [J]	1500	3500	100	500
τ_{pulse} [fs]	150	5000	1000	500
λ [nm]	1053	1053	1053	1053
N_{exc}	2.4×10^{-2}	1.9	1.1×10^{-2}	2.7×10^{-2}

We now turn to the case of high electron densities, which promises the strongest nuclear excitation according to Fig. 1. Experiments and simulations have shown that it is possible to isochorically heat targets at solid-state density to temperatures of a few hundred eV or even a few keV [60–62]. Since in this regime the heating of the target is mainly conducted by secondary particles, i.e., hot electrons generated in the laser-target interaction, a more sophisticated model is necessary compared to the low-density case. We have performed a one-dimensional particle-in-cell (PIC) simulation of a Nb solid target with 1 μm thickness and Nb density of $n_{\mathrm{nb}} = 5.5 \times 10^{22}$ cm^{-3} interacting with a high-power laser using the EPOCH code [63]. The isomer fraction of 10^{-5} is small enough to be neglected here in the determination of the plasma conditions. The laser has a Gaussian profile in time with peak intensity $I = 10^{18}$ W/cm^2, laser duration $\tau_{\mathrm{pulse}} = 500$ fs, and laser wavelength $\lambda = 800$ nm, respectively. A linear preplasma with the thickness of 0.5 μm is considered in front of the solid target. Ionization is not included explicitly in the simulation; as a representative order of the electron density, we fix the charge state to 10.

To include the effect of atomic ionization and recombination events, we averaged the raw data for electron temperature T_e and ion density n_i from the PIC simulation over 10 nm intervals, and used these values as input for the radiative-collisional model implemented in FLYCHK [48] to obtain charge state distributions and (corrected) electron densities. The electron density and temperature values are shown in the lower and middle panels of Fig. 3 for the time instants 2, 3, and 4 ps as a function of the target penetration depth x.

For the high-density region, we evaluate the NEEC rate as a function of target depth x and time t by inserting the PIC-simulation results for T_e and the corrected n_e values into Eq. (1). The plasma is assumed to be homogeneous only in the plane perpendicular to the x direction over the region of A_{focal}. We consider a laser pulse energy of 100 J, which leads for the pulse duration and laser intensity adopted in the PIC simulation to a focal spot area of approximatively 2×10^{-4} cm^2. Results for λ_{neec} are presented in the upper panel of Fig. 3. The rate is maximized at depths x with optimal plasma conditions for NEEC. The peak propagates through the target and disappears at around 4 ps as target heating leads afterwards to temperatures exceeding the optimal value. The analysis of the data sampled from 1 to 4 ps in 100-fs steps shows that the integrated NEEC rate reaches its maximum at 3.1 ps and drops roughly to half its value at 4 ps.

Using the regression curves for λ_{neec} calculated with the fitted n_{e} and T_e functions, we solve Eq. (2) in a two-step procedure to obtain N_{exc}. First, for each time instant t, the product of the NEEC rate and isomer density is integrated with respect to x over the whole target thickness d_t, and multiplied by the focal spot area A_{focal} to account for the perpendicular directions. Second, the outcomes of the spatial integration are interpolated as a function of time leading to $N_{\mathrm{exc}}(t)$, which is then inserted into the time integral in Eq. (2). For $t > 4$ ps, we extrapolate $N_{\mathrm{exc}}(t)$, assuming an exponential functional behavior initially following the slope at 4 ps. The time integration converges after approximatively 10 ps, leading to an excitation number of 1.8 isomers per pulse via NEEC, which is almost identical with the best value at low densities obtained with the PETAL parameters. With laser repetition rates of few Hz for 100 J pulses, the threshold of one isomer depletion per second should be reached providing a detectable signal. The experimental signature of the nuclear excitation would be a gamma-ray photon of approx. 1 MeV released in the decay cascade of the triggering level in ^{93}Mo. An evaluation of the plasma black-body and bremsstrahlung radiation spectra at this photon energy shows that the signal-to-background ratio is very high. Notable here is that in the high-density case, a 100 J laser, available at many facilities around the world, is competitive with a kJ-laser facility.

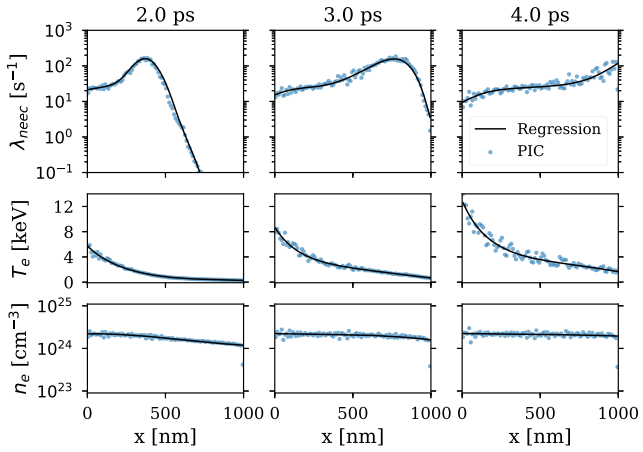

FIG. 3. Electron density, temperature and the NEEC rate based on the PIC simulation as functions of target depth x. The laser has peak intensity $I = 10^{18}$ W/cm^2 and $\lambda = 800$ nm wavelength. The raw data averaged over 10 nm intervals are presented together with a linear polynomial and a third order exponential fit for n_e and T_e, respectively. Regression curves for λ_{neec} calculated with the fitted n_e and T_e functions are shown in the upper graphs.

Tailoring the plasma conditions for NEEC promises a 12 orders of magnitude increase of the $^{93\mathrm{m}}$Mo depletion compared to the direct driving of the nuclear transition with an XFEL laser. An experimental proof of this scenario appears to be possible with present high-power optical lasers. The PIC simulation has been carried out in the direction with the smallest length scale of the plasma. Modeling the expansion in the perpendicular direction of the laser incidence, a roughly 10 to 100-times longer plasma lifetime can be expected to boost N_{exc}. A further enhancement can be achieved by employing a combination of optical and x-ray lasers as envisaged, for instance, at

Helmholtz International Beamline for Extreme Fields [64] at the European XFEL [65]. X-rays-generated inner shell holes could then provide the optimal capture state independently from the hot plasma conditions. We note, however, that further substantial improvements are required for practical energy storage applications. In our calculation, only a 10^{-10} fraction of the isomers in the plasma volume are depleted. In addition, the total isomer energy stored in the microscopic plasma volume is still far from typical requirements of macroscopic everyday life applications.

*yuanbin.wu@mpi-hd.mpg.de
†Jonas.Gunst@mpi-hd.mpg.de
‡Palffy@mpi-hd.mpg.de

[1] A. Di Piazza, C. Müller, K. Z. Hatsagortsyan, and C. H. Keitel, Rev. Mod. Phys. **84**, 1177 (2012).
[2] Linac Coherent Light Source—LCLS (2017).
[3] XFEL @ SACLA, Official Website (2017), http://xfel.riken.jp/eng/sacla/.
[4] ELI-beamlines L4 beam line webpage (2017), https://www.eli-beams.eu/en/facility/lasers/l4-10-pw-kj-beamline/.
[5] Petawatt Aquitaine Laser—PETAL webpage (2017), http://petal.aquitaine.fr/spip.php?lang=en.
[6] A. Casner, T. Caillaud, S. Darbon, A. Duval, I. Thfouin, J. P. Jadaud, J. P. LeBreton, C. Reverdin, B. Rosse, R. Rosch *et al.*, High Energy Density Phys. **17A**, 2 (2015).
[7] LULI2000 laser system webpage (2017), https://portail.polytechnique.edu/luli/en/facilities/luli2000/luli2000-laser-system.
[8] Central Laser Facility Vulcan laser webpage (2017), https://www.clf.stfc.ac.uk/Pages/Vulcan-laser.aspx.
[9] P. Mulser and D. Bauer, *High Power Laser-Matter Interaction* (Springer, Berlin, Heidelberg, 2010) Vol. 238.
[10] M. R. Harston and J. F. Chemin, Phys. Rev. C **59**, 2462 (1999).
[11] G. Gosselin and P. Morel, Phys. Rev. C **70**, 064603 (2004).
[12] G. Gosselin, V. Méot, and P. Morel, Phys. Rev. C **76**, 044611 (2007).
[13] P. Morel, V. Méot, G. Gosselin, D. Gogny, and W. Younes, Phys. Rev. A **69**, 063414 (2004).
[14] V. Méot, J. Aupiais, P. Morel, G. Gosselin, F. Gobet, J. N. Scheurer, and M. Tarisien, Phys. Rev. C **75**, 064306 (2007).
[15] P. Morel, V. Méot, G. Gosselin, G. Faussurier, and C. Blancard, Phys. Rev. C **81**, 034609 (2010).
[16] M. Comet, G. Gosselin, V. Méot, P. Morel, J.-C. Pain, D. Denis-Petit, F. Gobet, F. Hannachi, M. Tarisien, and M. Versteegen, Phys. Rev. C **92**, 054609 (2015).
[17] K. W. D. Ledingham, I. Spencer, T. McCanny, R. P. Singhal, M. I. K. Santala, E. Clark, I. Watts, F. N. Beg, M. Zepf, K. Krushelnick *et al.*, Phys. Rev. Lett. **84**, 899 (2000).
[18] T. E. Cowan, A. W. Hunt, T. W. Phillips, S. C. Wilks, M. D. Perry, C. Brown, W. Fountain, S. Hatchett, J. Johnson, M. H. Key *et al.*, Phys. Rev. Lett. **84**, 903 (2000).
[19] P. Gibbon, *Short Pulse Laser Interactions with Matter. An Introduction* (Imperial College Press, London, 2005).
[20] K. M. Spohr, M. Shaw, W. Galster, K. W. D. Ledingham, L. Robson, J. M. Yang, P. McKenna, T. McCanny, J. J. Melone, K.-U. Amthor, F. Ewald *et al.*, New J. Phys. **10**, 043037 (2008).
[21] G. Mourou and T. Tajima, Science **331**, 41 (2011).
[22] A. V. Andreev, R. V. Volkov, V. M. Gordienko, A. M. Dykhne, M. P. Kalashnikov, P. M. Mikheev, P. V. Nikles, A. B. Savel'ev, E. V. Tkalya, R. A. Chalykh *et al.*, J. Exp. Theor. Phys. **91**, 1163 (2000).
[23] A. V. Andreev, V. M. Gordienko, and A. B. Savel'ev, Quantum Electron. **31**, 941 (2001).
[24] C. Granja, J. Kuba, A. Haiduk, and O. Renner, Nucl. Phys. **A784**, 1 (2007).
[25] O. Renner, L. Juha, J. Krasa, E. Krousky, M. Pfeifer, A. Velyhan, C. Granja, J. Jakubek, V. Linhart, T. Slavicek *et al.*, Laser Part. Beams **26**, 249 (2008).
[26] F. Gobet, C. Plaisir, F. Hannachi, M. Tarisien, T. Bonnet, M. Versteegen, M. M. Aléonard, G. Gosselin, V. Méot, and P. Morel, Nucl. Instrum. Methods Phys. Res., Sect. A **653**, 80 (2011).
[27] S. M. Vinko, O. Ciricosta, B. I. Cho, K. Engelhorn, H.-K. Chung, C. R. D. Brown, T. Burian, J. Chalupsky, R. W. Falcone, C. Graves *et al.*, Nature (London) **482**, 59 (2012).
[28] J. Gunst, Y. A. Litvinov, C. H. Keitel, and A. Pálffy, Phys. Rev. Lett. **112**, 082501 (2014).
[29] J. Gunst, Y. Wu, N. Kumar, C. H. Keitel, and A. Pálffy, Phys. Plasmas **22**, 112706 (2015).
[30] P. Walker and G. Dracoulis, Nature (London) **399**, 35 (1999).
[31] A. Aprahamian and Y. Sun, Nat. Phys. **1**, 81 (2005).
[32] D. Belic, C. Arlandini, J. Besserer, J. de Boer, J. J. Carroll, J. Enders, T. Hartmann, F. Käppeler, H. Kaiser, U. Kneissl *et al.*, Phys. Rev. Lett. **83**, 5242 (1999).
[33] C. B. Collins, F. Davanloo, M. C. Iosif, R. Dussart, J. M. Hicks, S. A. Karamian, C. A. Ur, I. I. Popescu, V. I. Kirischuk, J. J. Carroll *et al.*, Phys. Rev. Lett. **82**, 695 (1999).
[34] D. Belic, C. Arlandini, J. Besserer, J. de Boer, J. J. Carroll, J. Enders, T. Hartmann, F. Käppeler, H. Kaiser, U. Kneissl *et al.*, Phys. Rev. C **65**, 035801 (2002).
[35] J. J. Carroll, Laser Phys. Lett. **1**, 275 (2004).
[36] A. Pálffy, J. Evers, and C. H. Keitel, Phys. Rev. Lett. **99**, 172502 (2007).
[37] G. D. Dracoulis, P. M. Walker, and F. G. Kondev, Rep. Prog. Phys. **79**, 076301 (2016).
[38] V. I. Goldanskii and V. A. Namiot, Phys. Lett. **62B**, 393 (1976).
[39] A. Pálffy, Contemp. Phys. **51**, 471 (2010).
[40] C. Chiara, in Topical Meeting on Isotope-Based Energy Sources, Washington, DC, 2017.
[41] S. A. Karamian and J. J. Carroll, Phys. At. Nucl. **75**, 1362 (2012).
[42] M. Polasik, K. Słabkowska, J. J. Carroll, C. J. Chiara, L. Syrocki, E. Węder, and J. Rzadkiewicz, Phys. Rev. C **95**, 034312 (2017).
[43] A. Pálffy, W. Scheid, and Z. Harman, Phys. Rev. A **73**, 012715 (2006).
[44] A. Pálffy, Z. Harman, and W. Scheid, Phys. Rev. A **75**, 012709 (2007).
[45] V. P. Krainov and M. B. Smirnov, Phys. Rep. **370**, 237 (2002).
[46] Experimental Nuclear Reaction Data—EXFOR (2017), https://www-nds.iaea.org/exfor/exfor.htm.
[47] M. Hasegawa, Y. Sun, S. Tazaki, K. Kaneko, and T. Mizusaki, Phys. Lett. B **696**, 197 (2011).

[48] H.-K. Chung, M. H. Chen, W. L. Morgan, Y. Ralchenko, and R. W. Lee, High Energy Density Phys. **1**, 3 (2005).
[49] K. G. Dyall, I. P. Grant, C. T. Johnson, F. A. Parpia, and E. P. Plummer, Comput. Phys. Commun. **55**, 425 (1989).
[50] J. C. Steward and K. D. Pyatt, Jr., Astrophys. J. **144**, 1203 (1966).
[51] C. Lin, G. Röpke, W.-D. Kraeft, and H. Reinholz, Phys. Rev. E **96**, 013202 (2017).
[52] S. X. Hu, Phys. Rev. Lett. **119**, 065001 (2017).
[53] J. Fuchs, P. Antici, E. d'Humières, E. Lefebvre, M. Borghesi, E. Brambrink, C. A. Cecchetti, M. Kaluza, V. Malka, M. Manclossi *et al.*, Nat. Phys. **2**, 48 (2006).
[54] Y. Wu and A. Pálffy, Astrophys. J. **838**, 55 (2017).
[55] F. Brunel, Phys. Rev. Lett. **59**, 52 (1987).
[56] G. Bonnaud, P. Gibbon, J. Kindel, and E. Williams, Laser Part. Beams **9**, 339 (1991).
[57] P. Gibbon and E. Förster, Plasma Phys. Controlled Fusion **38**, 769 (1996).
[58] Y. Ping, R. Shepherd, B. F. Lasinski, M. Tabak, H. Chen, H. K. Chung, K. B. Fournier, S. B. Hansen, A. Kemp, D. A. Liedahl *et al.*, Phys. Rev. Lett. **100**, 085004 (2008).
[59] D. F. Price, R. M. More, R. S. Walling, G. Guethlein, R. L. Shepherd, R. E. Stewart, and W. E. White, Phys. Rev. Lett. **75**, 252 (1995).
[60] A. Saemann, K. Eidmann, I. E. Golovkin, R. C. Mancini, E. Andersson, E. Förster, and K. Witte, Phys. Rev. Lett. **82**, 4843 (1999).
[61] P. Audebert, R. Shepherd, K. B. Fournier, O. Peyrusse, D. Price, R. Lee, P. Springer, J.-C. Gauthier, and L. Klein, Phys. Rev. Lett. **89**, 265001 (2002).
[62] Y. Sentoku, A. J. Kemp, R. Presura, M. S. Bakeman, and T. E. Cowan, Phys. Plasmas **14**, 122701 (2007).
[63] T. D. Arber, K. Bennett, C. S. Brady, A. Lawrence-Douglas, M. G. Ramsay, N. J. Sircombe, P. Gillies, R. G. Evans, H. Schmitz, A. R. Bell *et al.*, Plasma Phys. Controlled Fusion **57**, 113001 (2015); the EPOCH code was developed under the project that was in part funded by the UK EPSRC Grants No. EP/G054950/1, No. EP/G056803/1, No. EP/G055165/1, and No. EP/M022463/1.
[64] Helmholtz International Beamline for Extreme Fields at the European XFEL, Official Website (2017), https://www.hzdr.de/db/Cms?pNid=427&pOid=35325.
[65] European XFEL, Official Website (2017), http://www.xfel.eu/.